

# The Spitzer c2d Survey of Nearby Dense Cores: VI. The Protostars of Lynds Dark Nebula 1221

Chadwick H. Young

*Department of Physical Sciences, Nicholls State University, Thibodaux, Louisiana 70310*

Tyler L. Bourke

*Harvard-Smithsonian Center for Astrophysics, Cambridge, MA 02138, USA*

Michael M. Dunham

*Department of Astronomy, The University of Texas at Austin, Austin, Texas 78712–1083*

Neal J. Evans II

*Department of Astronomy, The University of Texas at Austin, Austin, Texas 78712–1083*

Jes K. Jørgensen

*Argelander Institut Für Astronomie, University of Bonn, Bonn, Germany*

Yancy L. Shirley

*Steward Observatory, University of Arizona, Tucson, AZ 85721*

Kaisa E. Young

*Department of Physical Sciences, Nicholls State University, Thibodaux, Louisiana 70310*

Christopher De Vries

*Department of Physics, Physical Science, and Geology, California State University  
Stanislaus, Turlock, California 95382*

Mark J. Claussen

*NRAO, P.O. Box 0, 1003 Lopezville Road, Socorro, NM 87801*

Victor Popa

*Department of Physical Sciences, Nicholls State University, Thibodaux, Louisiana 70310*

## ABSTRACT

Observations of Lynds Dark Nebula 1221 from the *Spitzer Space Telescope* are presented. These data show three candidate protostars towards L1221, only two of which were previously known. The infrared observations also show signatures of outflowing material, an interpretation which is also supported by radio observations with the Very Large Array. In addition, molecular line maps from the Five College Radio Astronomy Observatory are shown.

One-dimensional dust continuum modelling of two of these protostars, IRS1 and IRS3, is described. These models show two distinctly different protostars forming in very similar environments. IRS1 shows a higher luminosity and larger inner radius of the envelope than IRS3. The disparity could be caused by a difference in age or mass, orientation of outflow cavities, or the impact of a binary in the IRS1 core.

*Subject headings:* stars: formation, low-mass, L1221

## 1. Introduction

The story of star formation has long included the evolution from a starless core through the putative series of collapse stages (Shu et al. 1987). These stages include the Class 0-III, which are defined by various observational signatures and may represent times in the life of the protostar when the envelope and star have certain relative masses (Lada 1987). The *Infrared Astronomical Satellite (IRAS)* brought about much of what is known about the stars forming in dense cores, and, today, the *Spitzer Space Telescope* reveals new light from seen and unseen stars. Through data from *Spitzer*, new details about the collapse, accretion, disk formation, and ultimate birth of stars are being revealed.

In isolated, low-mass star formation, different cores provide different laboratories to study these processes. Some cores, such as L1014 (Young et al. 2004), seem to be forming only one star. However, many isolated cores are forming multiple star systems. For example IRAM 04191+1522 shows two distinct cores with 3 or more protostars (Andre et al. 1999; Dunham et al. 2006), and IRAS 16293-2422 is forming a close binary with a third star in the system (Jørgensen et al. 2005; Chandler et al. 2005; Loinard et al. 2007). These systems are important because they offer views of the impact that other protostars have on the evolution of their companions.

This paper presents new infrared, spectral line, and radio continuum observations of Lynds Dark Nebula 1221 (L1221). Descriptions of past observations of L1221 are in §2,

including molecular line observations and continuum data from the infrared to millimeter. A description of the observations and data reduction of L1221 with the *Spitzer Space Telescope* is in §3. Section 4 has results of the observations including luminosity, classification, and other details for the infrared sources detected by *Spitzer*. Section 5 describes the modelling of two protostellar systems in L1221. Finally, §6 offers a discussion and conclusions from the modelling.

## 2. Lynds Dark Nebula 1221

Lynd’s Dark Nebula 1221 (L1221) was first catalogued by Lynds (1962). She listed this dark core with an area of 0.020 square degrees and a relative opacity of 5 (on a scale of 1 to 6). The distance to L1221 is  $250 \pm 50$  pc (Yonekura et al. 1997). *IRAS* observed an infrared point source towards L1221, IRAS 22266+6845. Several authors have reported on observations of molecular line and (sub)millimeter detections. Young et al. (2006) and Wu et al. (2007) showed images at wavelengths of 350–850  $\mu\text{m}$ , and Caselli et al. (2002) reported their  $\text{N}_2\text{H}^+$  observations of L1221. Caselli et al. (2002) resolved only one extended core with a beamsize of  $1'$ . However, Young et al. (2006) and Wu et al. (2007) found that L1221 has two distinct cores, one in the north (L1221-SMM1) and one towards the south (L1221-SMM2), these cores are separated by  $50''$ . L1221-SMM1 is at the same position as IRAS 22266+6845.

Both L1221-SMM1 and SMM2 have very similar submillimeter fluxes; Young et al. (2006) calculated an isothermal mass of  $2.6 \pm 0.8 M_\odot$  for each individual core. These authors reported that L1221-SMM1, which was detected by *IRAS*, has a larger area than L1221-SMM2; Wu et al. (2007) gave major and minor axes for L1221-SMM1 ( $46''$  and  $33''$ ) and L1221-SMM2 ( $28''$  and  $19''$ ). These axes are measured from the  $2\text{-}\sigma$  contour level.

Several authors have observed the outflowing material from L1221. Based on single-dish observations, Umemoto et al. (1991) found a U-shaped outflow, presumably originating from IRAS 22266+6845. They concluded that the morphology of the outflow was due to interaction with a nearby dense ridge of material but that some external pressure (possibly magnetic fields) was also required to create the outflow of material seen from IRAS 22266+6845. Lee et al. (2002) reported, from their interferometric millimeter-wave observations (beamsize of  $10'' \times 10''$ ), the  $\text{J}=1 \rightarrow 0$  transition of CO and suggested that the U-shaped morphology was due to the interactions of multiple outflows, one of which originates with IRAS 22266+6845. Finally, Lee & Ho (2005) observed L1221 in several molecular lines (CO,  $\text{HCO}^+$ ,  $\text{N}_2\text{H}^+$ , and CS) with the Berkeley Illinois Millimeter Array (BIMA) and give 3 mm continuum fluxes for MM1 and MM2 (8 and 4 mJy, respectively, with beamsize  $4.7'' \times 3.8''$ ),

whose positions are coincident with SMM1 and SMM2. The continuum fluxes correspond to masses of 0.02 and 0.01  $M_{\odot}$  for MM1 and MM2, respectively. Lee & Ho (2005) provide a detailed model of the kinematics in L1221-MM1. They see evidence of a north-south outflow from L1221-MM2, but it is weak and not discussed in detail. They discuss the presence of a possible binary system in MM1, which is detected by these *Spitzer* observations, and drives an east-west outflow. The eastern component of this binary is coincident with the position of IRAS 22266+6845, but *IRAS* was unable to resolve the binary pair. Lee & Ho (2005) did not detect any continuum emission around the west object, for which they knew the position from these *Spitzer* observations, and concluded there was very little dust around it. Lee & Ho (2005) determined that the observations are best simulated by an infalling, slowly rotating, ringlike envelope around the the binary system in L1221-MM1.

### 3. Observations and Data Reduction

L1221 was observed with the *Spitzer Space Telescope* (Werner et al. 2004), as part of the Legacy Project “From Molecular Cores to Planet-forming Disks” (Evans et al. 2003, c2d). L1221 was observed with two instruments on *Spitzer*: the Infrared Array Camera (Fazio et al. 2004, IRAC) at 3.6 (IRAC band 1), 4.5 (IRAC band 2), 5.8 (IRAC band 3), and 8.0  $\mu\text{m}$  (IRAC band 4) and the Multiband Imaging Photometer for *Spitzer* (Rieke et al. 2004, MIPS) at 24 (MIPS band 1) and 70  $\mu\text{m}$  (MIPS band 2). The core was observed with IRAC on 19 July 2004 (Program ID (PID) 139, AOR key 0005165312) and with MIPS on 24 September 2004 (PID 139, AOR key 00094287636).

The IRAC observations of L1221 consisted of 8 pointings arranged in a 2 column by 4 row grid. Each pointing covers an area of about  $5' \times 5'$  for a total area of approximately  $10' \times 20'$ . The area was observed with 4 dithers, or individual images offset by approximately  $10''$ , with exposure times of 12 seconds each giving a total exposure time of 48 seconds.

The MIPS observation fields were smaller, focusing on the central parts of the L1221 core. The 24  $\mu\text{m}$  observations mapped an area of approximately  $5' \times 15'$ , or a 1 column by 3 row grid. One cycle (14 frames) of 3 second exposures was used at 24  $\mu\text{m}$  to obtain a total exposure time of 42 seconds. The 70  $\mu\text{m}$  camera mapped an area of about  $7.5' \times 15'$  in a  $3 \times 3$  grid. Each 70  $\mu\text{m}$  pointing had a total exposure time of 90 seconds obtained through three 10 frame cycles of 3 second exposures.

The IRAC and MIPS data were processed through the standard *Spitzer Science Center* pipeline (version S13 for IRAC and MIPS) creating Basic Calibrated Data (BCDs) before undergoing further processing in the c2d team internal pipeline. The c2d pipeline improves

the BCDs by removing instrumental artifacts in the data. A more complete description of this part of the data reduction is available in the c2d data delivery documentation (Evans et al. 2007). The improved data are then mosaicked to create a single map from the observations using the SSC software MOPEX. Sources are extracted and photometry is performed using a modified version of the DoPHOT software (Schechter et al. 1993). The modifications are described in Harvey et al. (2006).

In addition, the L1221 region was observed with the Very Large Array (VLA) in C array configuration on the days of 19 July, 2005 and 25 July, 2005 at 3.6 cm and 6.0 cm. Observations were centered on SSTc2d J222807.4+690039, which is called IRS3 in this paper. The correlator was setup with four IFs at adjacent frequencies to produce a continuum bandwidth of 172 MHz. The data were calibrated and imaged using the standard routines of *AIPS++*. The observations and data analysis are similar to the continuum observations of L1014 reported in Shirley et al. (2007).

Finally, observations of the  $\text{N}_2\text{H}^+$  ( $J = 1 \rightarrow 0$ ) and CS ( $J = 2 \rightarrow 1$ ) were taken with the 14 meter Five College Radio Astronomy Observatory (FCRAO). The beam size at these frequencies is about  $55''$ , and the velocity resolution is about 0.07 km/s. The observed velocity range for the  $\text{N}_2\text{H}^+$  is from -5.1 to -3.7 km/s; the line width is  $0.68 \pm 0.04$  km/s. The observed velocity range for CS is -5.9 to -2.9 km/s; the line width is  $1.5 \pm 0.5$  km/s. Multiple pointings were observed to create maps of the region in the the  $\text{N}_2\text{H}^+$  and CS transitions, which are in the 3 mm atmospheric window. These observations will be described in a separate paper (De Vries et al. in prep.).

#### 4. Results

The images of this region are shown in Figures 1, 2, 3, and 4. Figure 1 has the IRAC 3.6, 4.5, and  $8.0 \mu\text{m}$  observations represented as blue, green, and red. Figure 2 has the same color scheme but zoomed in to the region of L1221-SMM1 and SMM2. Three infrared sources—IRS1, IRS2, and IRS3—appear to be associated with L1221. IRS1 and IRS2 appear unresolved in Figures 1 and 2 because the source is overexposed. The positions of the three sources are labeled in Figure 3, which show the IRAC and MIPS data, separately, for the 3 infrared sources. Finally, Figure 4, has the submillimeter continuum (850 and  $350 \mu\text{m}$ ) and FCRAO molecular line observations overlaid on the  $8.0 \mu\text{m}$  grayscale image. Observed fluxes for the infrared sources are in Table 1.

SSTc2d J222803.0+690117 (hereafter, L1221-IRS1), was detected at all *Spitzer* bands and was also detected by *IRAS* (IRAS 22266+6845) and *2MASS* (2MASS 22280298+6901166).

L1221-IRS1 was also detected in the near-infrared by Hodapp (1994) and catalogued as an outflow driver. This object has  $[4.5] - [8.0] = 1.4$  and  $[8.0] - [24] = 4.4$ , which qualifies it as a candidate young stellar object (YSOc) according to the criteria given in Harvey et al. (2006); it is also a YSOc after the scheme in Harvey et al. (2007). Further evidence of its nature include coincidence with dense gas and evidence that it drives an outflow (Lee & Ho 2005). The fluxes for L1221-IRS1 (1.25 to 850  $\mu\text{m}$ , as in Table 1) give  $L_{\text{bol}}=1.8 L_{\odot}$  and  $T_{\text{bol}}=250$  K, which classifies it as a Class I object, according to the scheme developed by Myers & Ladd (1993); these were calculated using the trapezoidal method of integration. The spectral index, as defined by Lada (1987), is  $\alpha = 0.81$ , which classifies this object as a Class I protostar (Greene et al. 1994). The spectral index is calculated as described in the final delivery document for the c2d Legacy Program (Evans et al. 2007).

There is a source  $7''$  (1750 AU) west of L1221-IRS1, SSTc2d J22801.8+690119 (hereafter, L1221-IRS2). IRS1 and IRS2 were not resolved by *IRAS*; however, the coordinates for the *IRAS* source are closer to IRS1 than IRS2 ( $4''$  versus  $17''$ ). The separation between IRS1 and IRS2 is about equal to the resolution of *2MASS*, so IRS2 is not included in the *2MASS* catalogs. Hodapp (1994) detected several near-infrared sources towards L1221. The brightest is clearly associated with L1221-IRS1; they also detect faint emission from IRS2. The separation between IRS1 and IRS2 is smaller than the resolution for MIPS at 70  $\mu\text{m}$ ,  $17''$ . However, the source position for the 70  $\mu\text{m}$  detection is coincident with L1221-IRS1. Therefore, an upper limit of about 300 mJy at 70  $\mu\text{m}$  can be assumed for L1221-IRS2; a flux larger than this value would cause a shift in the source position towards L1221-IRS2 (T. Brooke priv. comm.). Additionally, the 24  $\mu\text{m}$  flux for L1221-IRS2 was not listed in the c2d source catalogs, so the IRAC source positions were input to MOPEX, which gave the 24  $\mu\text{m}$  flux of 480 mJy (Brooke priv. comm.). L1221-IRS2 has  $[4.5] - [8.0] = 2.1$  and  $[8.0] - [24] = 2.9$ , both of which qualify it as a YSOc (Harvey et al. 2006); it is also a YSOc after the scheme in Harvey et al. (2007). The bolometric luminosity (from 3.6-24  $\mu\text{m}$ ) is  $0.4 L_{\odot}$  and  $T_{\text{bol}} = 450$  K (Class I). The spectral index is  $\alpha = -0.05$ ; L1221-IRS2 is considered a “flat-spectrum” protostar by this index (Greene et al. 1994). Of course, the spectral energy distribution is poorly sampled, and these classifications may change with future observations at different wavelengths.

*Spitzer* detected a southeastern source at all wavelengths (SSTc2d J22807.4+690039), hereafter L1221-IRS3. This object is about  $50''$  (12500 AU) from L1221-IRS1 and was undetected by *IRAS* or *2MASS*. Figures 1 and 2 show 4.5  $\mu\text{m}$  (green) emission emanating north and south of IRS3. This emission has been shown to indicate outflowing material (Noriega-Crespo et al. 2004). Indeed, Lee & Ho (2005) detected a weak, N-S outflow from SMM2. Lee & Ho (2005) proposed that this outflow probably emanates from IRS3.

L1221-IRS3 has  $[4.5] - [8.0] = 1.1$  and  $[8.0] - [24] = 5$ , which qualifies it as a YSOc; it is also a YSOc after the scheme in Harvey et al. (2007). The fluxes give  $L_{bol} = 0.8 L_{\odot}$  and  $T_{bol} = 68$  K over all observed wavelengths (3.6-850  $\mu\text{m}$ ), which classifies it as a Class 0 object ( $<70$  K). The spectral index is  $\alpha = 0.99$  (Class I); the spectral index does not define the Class 0, so these disparate classifications are not necessarily inconsistent.

The spectral energy distributions for L1221-IRS1, IRS2, and IRS3 are shown in Figure 5. IRS1 shows more emission at shorter wavelengths but is very similar to IRS3 in the longer wavelengths, suggesting their envelopes, traced by submillimeter emission, are very similar.

L1221-IRS3 was the only source of these three that was detected at either 3.6 or 6.0 cm with the VLA. This result agrees with the previous VLA image at 3.6 cm of the L1221 region made by Rodríguez & Reipurth (1998). Rodríguez & Reipurth (1998) detect an unresolved 3.6 cm continuum source that is coincident with L1221-IRS3 ( $22^h 55^m 7.36^s +69^\circ 00' 39.9''$ , J2000.0) with a flux of  $210 \pm 20 \mu\text{Jy}$ . L1221-IRS3 was detected again in the 2005 VLA observations with at 3.6 cm and 6.0 cm with fluxes of  $177 \pm 24 \mu\text{Jy}$  and  $192 \pm 27 \mu\text{Jy}$  respectively. These flux levels are within a factor of 2 of the centimeter fluxes observed toward L1014-IRS, which has 3.6 cm and 6.0 cm fluxes of  $111 \pm 8 \mu\text{Jy}$  and  $88 \pm 11 \mu\text{Jy}$ , respectively (Shirley et al. 2007). Also, the 3.6 cm flux for L1221 agrees with the value quoted by Rodríguez & Reipurth (1998). The spectral index between 3.6 cm and 6.0 cm is  $-0.16 \pm 0.54$ . This spectral index is consistent with the index for optically thin free-free emission, although a steeper negative or positive spectral index cannot be ruled out. Since there is strong evidence from the IRAC images of a molecular outflow from a central protostar at L1221-IRS3, the most likely explanation for the observed centimeter emission is shock-ionization from interaction of the protostellar jet from IRS3 with the surrounding material in the envelope (Curiel et al. 1987, 1989; Anglada 1995; Shang et al. 2004).

Finally, there is a fourth infrared source, which was detected from 3.6-70  $\mu\text{m}$ . SSTc2d J222815.1+685930 is an object about  $2.2'$  southeast from the L1221 core. It is included here because it was one of three sources, including L1221-IRS1 and L1221-IRS3, that was detected at 70  $\mu\text{m}$ . The c2d catalogs list this object as very likely a background galaxy based on color-magnitude cutoffs from *SWIRE* (Evans et al. 2007; Harvey et al. 2007; Lonsdale et al. 2003). Fluxes for this source are given in Table 1.

## 5. 1-Dimensional Models

Physical models for L1221-IRS1 and L1221-IRS3 were created to best match the fluxes from 3.6 to 850  $\mu\text{m}$ ; because the SED of L1221-IRS2 is poorly sampled, there was no at-

tempt to model its emission. The models are one-dimensional and included a central star, a disk, and envelope. The disk is included in this one-dimensional model as discussed in Butner et al. (1994) and Young & Evans (2005). The radiative transfer was calculated using Dusty (Ivezić et al. 1999).

The model parameters, which were allowed to vary, include the stellar luminosity ( $L_*$ ), the disk luminosity ( $L_D$ ), the stellar photospheric temperature ( $T_*$ ), the inner radius of the envelope ( $r_i$ ), and the power-law density distribution of the envelope ( $p$ ).

The other parameters of the model, which were not changed, include the disk inner and outer radii ( $R_i$  and  $R_o$ ), the power-law surface density distribution of the disk, the power-law temperature distribution of the disk ( $q$ ), properties of dust in the envelope, the outer radius of the envelope ( $r_o$ ), and the total mass of the envelope ( $M_{env}$ ).

For the disk parameters, default values for all except the disk luminosity,  $L_D$ , have been adopted. The surface density power law index is  $p = 1.5$ , and the temperature power law index is  $q = 0.5$ . The former is in accordance with the density structure for a disk in vertical hydrostatic equilibrium (Chiang & Goldreich 1997), and the latter is chosen to simulate the effects of flaring and disk accretion (Butner et al. 1994; Kenyon & Hartmann 1987). The inner radius of the disk is set to where the dust is heated to greater than 2000 K and is, presumably, destroyed. The outer radius is assumed to be 5 AU; this is similar to the disk radius, based on the centrifugal radius, used for IRAM 04191+1522 (Dunham et al. 2006). The effect of the disk outer radius ( $R_o$ ) is discussed in §5.3. The scale of the power-law density distribution was set by assuming the disk has a mass of  $0.005 M_\odot$ , which is similar to the assumed disk for IRAM 04191+1522 (Dunham et al. 2006), a source that seems to be similar to L1221-IRS3. In fact, the mass of the disk has little effect on the model. The disk luminosity,  $L_D$ , arises because of accretion onto the disk and is a free parameter in these models. Basically,  $L_D$  has to be tuned in order to match the 24 and 70  $\mu\text{m}$  observations. As discussed in Young & Evans (2005),  $L_D$  is not indicative of the mass of the disk; it is simply set to a particular value so as to match the observations.

The 850  $\mu\text{m}$  flux is least susceptible to geometric effects because the envelope is optically thin at this wavelength. Therefore, this flux was used to constrain the mass of the envelope. The fiducial density was set, depending on the value for the inner radius, such that the modelled 850  $\mu\text{m}$  flux would match the observed flux.

Because the shape of the envelope’s density distribution is not known, a power-law density distribution,  $n(r) = \left(\frac{r}{r_f}\right)^{-p}$  ( $r_f = 1000$  AU), with indices of  $p = 1.5$  or  $p = 2.0$  is assumed. Young et al. (2003) found a median  $p$  of 1.8; indeed, most studies have found an average power-law index to be between 1.5 and 2.0 (Shirley et al. 2002; Motte & André



2001).

The outer radius of the envelope is chosen to be  $r_o = 5000$  AU. The outer radius is not easily constrained from submillimeter observations. However, Wu et al. (2007) gave the major axes of IRS1 and IRS3 ( $46''$  and  $28''$ ; 12000 and 7000 AU) at the  $2\text{-}\sigma$  level. These sizes correspond to outer radii of 6000 and 3500 AU. Therefore, the outer radius is set to the average of these values (5000 AU) for both cores. Wu et al. (2007) also warned that SHARC-II is not sensitive to extended emission, so the reported values potentially underestimate the submillimeter size of the cores. However, the cores are separated by  $50''$  in the plane of the sky, which corresponds to 12500 AU. Then, it is reasonable to assume the outer radii do not exceed 6000 AU.

For the dust properties, the opacities calculated by Ossenkopf & Henning (1994) from the fifth column of Table 1 in their paper (so-called OH5 dust) were used. These data have been extended to a greater range of wavelengths as described in Young & Evans (2005). The scattering of light by the dust grains is ignored, as discussed in Young & Evans (2005). The impact of this assumption is discussed in §5.3.

The envelope is heated externally by the interstellar radiation field (ISRF). As described in Young & Evans (2005), the ISRF has been attenuated by the opacity due to Draine & Lee (1984) dust with  $A_V = 3$ . This simulates the effect of low density material in the surrounding environs of a star-forming core.

To determine the best-fit model, the reduced  $\chi^2$  was calculated over all *Spitzer* wavelengths as such

$$\tilde{\chi}^2 = \frac{1}{k} \sum_i \frac{[S_\nu^{obs}(\lambda_i) - S_\nu^{mod}(\lambda_i)]^2}{[\sigma_\nu(\lambda_i)]^2}, 3.6 \leq \lambda_i \leq 70\mu m \quad (1)$$

The degrees of freedom ( $k = n - m$ ) is the difference between the number of free parameters ( $m = 4$ ) and the number of data points in the SED ( $n = 9$ ).

Then, four different grids were examined to find the parameters that give the lowest  $\tilde{\chi}^2$  values. These four grids cover the following parameter spaces:  $L_* - L_D$ ,  $L_* - r_i$ ,  $T_* - r_i$ , and  $T_* - L_*$ , for grids 1 through 4, respectively.

The  $\tilde{\chi}^2$  values for grids 1 and 2 are plotted as greyscale in Figure 6 for L1221-IRS1 and Figure 7 for L1221-IRS3. Grids 3 and 4, which are not shown, pinpoint values for  $r_i$  and  $L_*$  that are similar to those found in grids 1 and 2. In addition, grids 3 and 4 probe the effective temperature of the protostar. These models are insensitive to stellar temperature. The envelope is optically thick at the shorter wavelengths, so all of the stellar photospheric radiation is reprocessed. The stellar temperature, then, is set at 3000 K, which is representative for a late-M dwarf. Because the  $\tilde{\chi}^2$  plots for Grids 3 and 4 are redundant,

they are not shown, but the minimum  $\tilde{\chi}^2$  values for several parameters from all grids are plotted in Figures 8 and 9.

### 5.1. L1221-IRS1

L1221-IRS1 was detected by *IRAS*, *Spitzer*, *2MASS*, *SHARC-II*, and *SCUBA*. However, the near-infrared data are not well fitted by a one-dimensional model, so the *2MASS* observations are not used in calculating  $\tilde{\chi}^2$  (as given by equation 1).

L1221-IRS1 has a nearby companion, L1221-IRS2, about  $7''$  away, which corresponds to 1750 AU. However, L1221-IRS2 is much less luminous than L1221-IRS1; it was not resolved at  $70\ \mu\text{m}$ , but there is an upper limit on the  $70\ \mu\text{m}$  flux of 300 mJy. Additionally, Lee & Ho (2005) detected no continuum 3 mm emission from L1221-IRS2 and concluded that there was probably very little dust surrounding this object. Hodapp (1994) detected emission from both IRS1 and IRS2, though the emission from IRS2 was very faint.

Because IRS2 is much less luminous, it is not included in the model of IRS1 and its surrounding envelope. It is, of course, possible that L1221-IRS2 is not even associated with the core and is simply a background object. However, it is a YSOc, so its impact as a potential binary companion will be discussed in section 6.

Initially, values for the model parameters that produced a reasonably good fit to the data were assumed:  $r_i = 1000\ \text{AU}$ ,  $L_* = 1\ L_\odot$ ,  $L_D = 1\ L_\odot$ , and  $T_* = 3000\ \text{K}$ ; these are the default values for the free parameters. When allowed to vary, these parameters were set in the following ranges:  $r_i = 250 \rightarrow 2500\ \text{AU}$ ,  $L_* = 0.5 \rightarrow 5\ L_\odot$ ,  $L_D = 0.5 \rightarrow 5\ L_\odot$ , and  $T_* = 1000 \rightarrow 20000\ \text{K}$ .

The fiducial density, at  $r_f = 1000\ \text{AU}$ , was set such that the total envelope mass was always a certain value to match the  $850\ \mu\text{m}$  flux (2 Jy). For the models with  $p = 1.5$ , the mass is  $1.1\ M_\odot$ ; when  $p = 2.0$ ,  $M_{\text{env}} = 0.9\ M_\odot$ . Also, when the envelope has different inner radii, the fiducial densities must be adjusted to produce these envelope masses. For inner radii from 250 to 2500 AU, the range of fiducial densities were  $1.8 \times 10^6$  to  $2.7 \times 10^6\ \text{cm}^{-3}$  for the  $p = 1.5$  models and  $2.2 \times 10^6$  to  $4.2 \times 10^6\ \text{cm}^{-3}$  for the  $p = 2.0$  models.

Figure 6 shows greyscale plots with the  $\tilde{\chi}^2$  values of models with  $p = 1.5$  and  $p = 2.0$ . Grid 1 shows a range of appropriate luminosities for the star and disk. Grid 2 effectively pinpoints one valid inner radius and stellar luminosity.

For each set of models, the minimum  $\tilde{\chi}^2$  values for the total internal luminosity ( $L_{\text{int}}$ ) and  $r_i$  are plotted in Figure 8. These graphs show which of these values gave the best  $\tilde{\chi}^2$

and were used in determining the best-fit parameters.

To determine the appropriate model parameters, the inner radius is selected from Grid 2. Then, the inner radius, which gives the lowest  $\tilde{\chi}^2$ , is taken from Grid 3 (see Figure 8). Averaging the values for  $r_i$  gives the best-fit model parameter as reported in Table 2. There is some ambiguity in the knowledge of  $L_*$  and  $L_D$ . As shown in Grid 1 of Figure 6, the best-fit stellar luminosity depends upon the chosen disk luminosity. Therefore, the sum  $L_* + L_D$  ( $L_{int}$ ) is constrained with Grid 1 and equally apportioned for  $L_*$  and  $L_D$ .

The best-fit parameters are given in Table 2. The model with  $p = 2.0$  has a slightly better  $\tilde{\chi}^2$  value; however, both models have fairly high  $\tilde{\chi}^2$  values ( $\sim 50$ ). For both  $p = 1.5$  and  $p = 2.0$ , the inner radius ( $r_i$ ) is 1000 AU; the total internal luminosity is  $2.6 L_\odot$ . The spectral energy distributions for these two models are shown in the upper panels of Figure 10. The dotted line in these plots represents the spectral energy distribution (SED) of the star and disk, excluding the envelope; the solid line is the SED of the star, disk, and envelope system. The error bars represent the observed fluxes.

The models often did not match the MIPS data, so  $\tilde{\chi}_{MIPS}^2$ , which only includes  $\lambda_i = 24$  and  $70 \mu\text{m}$ , is used to find the model that best fits the MIPS data.  $L_{int}$  was held constant while  $L_D$  was varied to optimize  $\tilde{\chi}_{MIPS}^2$  while the envelope parameters ( $r_i$ ,  $p$ , and  $n_f$ ) are the same as in Table 2. These models are represented by the long dashed line in Figure 10. For  $p = 1.5$ ,  $L_* = 1.3$  and  $L_D = 1.9 L_\odot$ ; for  $p = 2.0$ ,  $L_* = 1.3$  and  $L_D = 1.7 L_\odot$ ; the best  $\tilde{\chi}_{MIPS}^2$  values were for the  $p = 1.5$  model. In both cases, the  $70 \mu\text{m}$  observations are better matched, but the  $24 \mu\text{m}$  is still underestimated by the model. As  $L_D$  increases, the  $70 \mu\text{m}$  flux increases at a greater rate than the  $24 \mu\text{m}$  flux because of the higher extinction at  $24 \mu\text{m}$ . Therefore, as  $L_D$  is increased, the  $70 \mu\text{m}$  flux is increased, but the  $24 \mu\text{m}$  remains about the same. Of course, the IRAC fluxes are also overestimated by these models, since their values were not considered in calculating  $\tilde{\chi}_{MIPS}^2$ . This effect is prevalent in all four models. A more realistic and two-dimensional treatment of the disk is necessary to remove this effect.

## 5.2. L1221-IRS3

L1221-IRS3 is the only infrared source detected in the southern submillimeter core, L1221-SMM2. This is the first report of its infrared detection. Modelling of IRS3 follows closely the process for IRS1. The same default values for disk parameters (except  $L_D$  and  $R_i$ ), dust opacity (OH5), power-law density profiles ( $p = 1.5$  and  $2.0$ ), and heating by the ISRF as used for IRS1 were kept for IRS3.

Initially, values for the model parameters that produced a reasonably good fit to the

data were assumed:  $r_i = 100$  AU,  $L_* = 0.4 L_\odot$ ,  $L_D = 0.4 L_\odot$ , and  $T_* = 3000$  K; these are the default values for the free parameters. When allowed to vary, these parameters were set in the following ranges:  $r_i = 50 \rightarrow 750$  AU,  $L_* = 0.1 \rightarrow 2 L_\odot$ ,  $L_D = 0.1 \rightarrow 2 L_\odot$ , and  $L_* = 500 \rightarrow 5000$  K.

Then, the fiducial density ( $n_f$ ) was set to match the modelled and observed  $850 \mu\text{m}$  fluxes. The  $850 \mu\text{m}$  flux is dependent on the dust mass and temperature. The models with different values for  $p$  have differing temperature distributions. Therefore, one must choose 2 envelope masses that create an  $850 \mu\text{m}$  flux that best matches the observations. For the  $p = 1.5$  models, the envelope mass is  $1.75 M_\odot$ . When  $p = 2.0$ ,  $M_{env} = 1.25 M_\odot$ . The steeper density profile has higher temperatures, so a smaller dust mass is required to produce the  $850 \mu\text{m}$  flux.

Because the inner radius changes in these models, different fiducial densities are required to create an envelope with these masses. For inner radii from 50 to 750 AU, the range of fiducial densities (at  $r_f = 1000$  AU) were  $2.8 \times 10^6$  to  $2.9 \times 10^6 \text{ cm}^3$  for the  $p = 1.5$  models and  $3.0 \times 10^6$  to  $3.5 \times 10^6 \text{ cm}^3$  for the  $p = 2.0$  models.

The  $\tilde{\chi}^2$  two-dimensional plots are in Figure 7. The plots of minimum  $\tilde{\chi}^2$  are in Figure 9. Analyzing these data in the same way as for IRS1, the best-fit parameters were found, which are given in Table 2, are as follows. For  $p = 1.5$ ,  $r_i = 100$  AU, and  $L_{int} = 0.4 L_\odot$ . For  $p = 2.0$ ,  $r_i = 150$  AU and  $L_{int} = 2.2 L_\odot$ . The model with  $p = 2.0$  has a slightly better  $\tilde{\chi}^2$  value, though both models have fairly high  $\tilde{\chi}^2$  values. The spectral energy distributions for these two models are shown in the lower panels of Figure 10.

As discussed for IRS1, models considering just  $\tilde{\chi}_{MIPS}^2$  were calculated and are shown by the long-dashed lines in Figure 10. The best-fit models have the same parameters for the envelope ( $r_i$ ,  $p$ , and  $n_f$ ) as those in Table 2, but their disk luminosities are varied. The new parameters are as follows: for  $p = 1.5$ ,  $L_{int} = 0.2$  and  $L_D = 1.0 L_\odot$ ; for  $p = 2.0$ ,  $L_{int} = 1.1$  and  $L_D = 0.4 L_\odot$ . The best  $\tilde{\chi}_{MIPS}^2$  values were for the  $p = 1.5$  model.

The modelled  $L_{int}$  is significantly different than the observed bolometric luminosity ( $0.8 L_\odot$ ). This discrepancy highlights the importance of far-infrared observations. For the  $p = 2.0$  model, the luminosity between  $75$  and  $350 \mu\text{m}$  is  $1.9 L_\odot$ . However, this spectral range, which is the peak of the SED, is not sampled with observations, so the modeled  $L_{bol}$  is much larger than the observed  $L_{bol}$ .

### 5.3. Constraint of Internal Luminosity

These models are one-dimensional and insufficient to fully describe the physical nature of these systems. One-dimensional models are not equipped to simulate the effects of a more realistic disk or scattering by dust grains. These shortcomings cause an uncertainty in the modelling of fluxes at shorter wavelengths, especially in the near-infrared. As such, the NIR fluxes have not been included in the  $\chi^2$  calculations. However, one-dimensional models are useful because they constrain the luminosity of the internal source. Either including scattering of light or altering disk parameters does not affect the conclusions about internal luminosity.

Because dust grains preferentially forward scatter light, the one-dimensional code, Dusty, is unable to properly account for scattering (Young & Evans 2005). Dunham et al. (in prep.) have created dust opacities that account for scattering by adding the scattering and absorption opacities. This is not an entirely reasonable assumption, but Dunham et al. (in prep.) have shown that this method offers good agreement with two-dimensional models, which are able to treat scattering in a more correct manner.

Figure 11 shows the best-fit models, whose parameters are given in Table 2, as a dotted line. The solid line in Figure 11 shows the best-fit model when these new opacities are used (as in Dunham et al. (in prep.)). The new opacities allow for a better fit at shorter wavelengths, especially in the near-infrared. However, the internal luminosity for IRS1 and IRS3 are changed very little; the inner radii for both sources are increased by, at least, a factor of 2.

Dunham et al. (2006) concluded, similarly, that the luminosity of the internal source is well-constrained by one-dimensional models. The results for  $L_{int}$  of IRS1 and IRS3 are robust, but the inner radii are dependent on a variety of parameters related to the disk, dust opacities, and other two-dimensional effects.

In addition, the disk is important to the overall fit of the model, but certain parameters of the disk, such as its outer radius, do not have a large impact on the best-fit models. A small disk outer radius (5 AU) has been adopted for the models of IRS3 and IRS1, but the radius of the disk has little effect on the modelled SED. Figure 12 has the best-fit models for IRS1 and IRS3 (with  $p = 1.5$ ). In addition, this figure shows models with disk outer radii of 50 and 500 AU. Though the disk spectra (dashed line) are markedly different, the SED of the protostar, disk, and envelope (solid line) are all about the same. Clearly, the disk plays an important role in the mid-infrared portion of the SED; in fact, these models underestimate the 24  $\mu\text{m}$  flux. However, further observations to constrain disk parameters and higher-dimensional models are needed for more certain conclusions. Observations with

Sofia and Herschel will provide better sampling of the SED, and submillimeter interferometry will be useful to constrain the disk masses and sizes in this system.

In comparison, Dunham et al. (2008) found a relationship between  $L_{int}$  and the flux at  $70\ \mu\text{m}$ ; the relationship is found to be reliable within a factor of  $\sim 2$ . Based on the  $70\ \mu\text{m}$  flux for IRS1, the derived  $L_{int}$  is  $1.1\ L_{\odot}$ , while the model suggests  $L_{int} = 2.6\ L_{\odot}$ . The Dunham et al. (2008) relationship derives  $0.8\ L_{\odot}$  for IRS3, while the model gives a range for  $L_{int}$  from  $0.4$  to  $2.2\ L_{\odot}$ , depending on the density profile for the envelope. Given the uncertainty in the Dunham et al. (2008) relationship, the modeled luminosities are consistent with those derived from the  $70\ \mu\text{m}$  flux.

In conclusion, results for the internal luminosity are fairly robust. They are not affected by changes either in the disk or the effects due to scattering, even though these changes can drastically affect the near-infrared portion of the overall spectrum.

## 6. Discussion and Conclusions

The L1221 star-forming region presents an example of stars forming differently in very similar environments. L1221-SMM1 and SMM2 are, presumably, both part of the same region and are separated, in the plane of the sky, by approximately  $50''$ . Their  $850\ \mu\text{m}$  fluxes are identical, so their total masses are also similar, though their submillimeter sizes and, possibly, density profiles, are different. Also, the two cores appear to be a part of the same molecular core, as in Figure 4, and dark cloud (Lynds 1962). These two cores, because of their close proximity ( $50'' = 12500\ \text{AU}$ ), are likely to be affected by the same large-scale dynamical effects due to nearby stars and astronomical events; they are also likely to have been born out of a very similar makeup of materials. In short, L1221-SMM1 and SMM2 should provide similar environments for the formation of stars.

L1221 is not unique. A number of cores have been found to be home to multiple protostars in different stages of formation. Duchêne et al. (2007) found multiplicity rates of 30-50% among protostellar systems with separations of up to  $1400\ \text{AU}$ ; the protostars included Class I and flat-spectrum sources in several molecular clouds. IRAM 04191+1422 has several similarities with L1221, as well. Andre et al. (1999) discovered this very-low luminosity object (VeLLO) (Dunham et al. 2006) about  $1'$  ( $8400\ \text{AU}$ ) from IRAS 04191+1523, a Class I protostar. Like L1221-IRS1, IRAS 04191+1523 also has two sources, unresolved by *IRAS*, that are  $6.5''$  apart. These sources were resolved by IRAC and 2MASS but not MIPS or SCUBA (Dunham et al. 2006). This star-forming region is similar to L1221 in that it appears to have several protostars at different stages of evolution. L1251B is another

star-forming region that is home to different classes of protostars including four Class O/I stars (Lee et al. 2006). Finally, Yun & Clemens (1995) found two near-infrared sources in the star-forming core CB230. These supposed protostars are separated by  $11''$ . Other examples of pairs include BHR 71 (Bourke et al. 2001) and CG30 (Chen et al. 2008). These cores are examples of sources similar to the L1221 star-forming region in that they are all forming multiple protostars that are, presumably, at differing stages of evolution.

IRS1 and IRS3, the dominant infrared sources in SMM1 and SMM2, are clearly not as similar as their host cores. First, their luminosities are different. L1221-IRS1 has an internal luminosity, including the disk and stellar components, of  $2.6 L_{\odot}$ , while L1221-IRS3 has  $L_{int} = 2.2$  or  $0.4 L_{\odot}$ , depending on the density profile. The observed infrared luminosity (with  $\lambda \leq 70 \mu\text{m}$ ) for IRS1 is  $1.6 L_{\odot}$  and for IRS3 is  $0.4 L_{\odot}$ .

The luminosity is the result of accretion onto the disk and star. Since each core likely has similar temperature and turbulence, the accretion rates for IRS1 and IRS3 are probably very similar. Because accretion luminosity is directly proportional to the protostar’s mass, IRS1 is potentially about 4 times more massive than IRS3.

However, IRS3, for the two best-fit models, has a range of possible luminosities from  $0.4$  to  $2.2 L_{\odot}$ . Additional observations in the wavelength range from  $70$  to  $350 \mu\text{m}$  (such as with Herschel) would easily discern the appropriate internal luminosity since the models are quite different in this portion of the SED.

Current submillimeter ( $450$  and  $850 \mu\text{m}$ ) maps, made with the scan map technique on SCUBA, have poor signal-to-noise ratios and are insufficient to determine the shape of the density profile for these cores. More sensitive observations of the extended submillimeter emission are needed to determine the density profile of the envelope (Shirley et al. 2002).

The envelopes’ inner radii of the L1221-IRS3 and L1221-IRS1 models are distinctly different. L1221-IRS3 requires  $r_i = 100$  or  $150$  AU; L1221-IRS1 needs a much larger inner radius ( $1000$  AU). Two scenarios can explain this disparity. First, L1221-IRS3 might be at a much earlier stage in its collapse, and the inner radius has not expanded as predicted by Terebey, Shu, & Cassen (1984). Another alternative is that the binary possibly in L1221-SMM1 (IRS1 and IRS2) could have evacuated the cavity of some fraction of the material. The separation of this binary is  $7''$ , which corresponds to  $1750$  AU. Jørgensen et al. (2005) found a similarly large inner radius for IRAS 16293-2422 and reported that the radius of the inner cavity was comparable to the centrifugal radius. Lee & Ho (2005) reported a “hole” in the  $\text{N}_2\text{H}^+$  emission, which could suggest a cleared out cavity in the center of the core. However, this could also be a chemical effect as discussed in Jørgensen et al. (2004) and as observed by Jørgensen (2004).

For IRAS 16293-2422, Jørgensen et al. (2005) suggested a two-dimensional model that used a much smaller inner radius when outflow cavities were instituted and when the protostar was viewed down the outflow cavity. They found that the mid-infrared fluxes were greatly increased when observed down the outflow cavity. A similar scenario might apply for L1221 IRS1 and IRS3. IRS1 might be observed pole-on while IRS3 is edge-on. However, because of the bipolar nature of IRS1 (Lee & Ho 2005), this is unlikely.

The chief results of these models include these conclusions about the luminosities and envelope inner radii. The luminosity of each core is easily constrained with a one-dimensional model because most of the luminosity is emitted in the far-infrared, which is largely unaffected by the central star’s near-infrared spectrum; the one-dimensional model is sufficient also because the re-radiated emission is thin. Given the same data, even a more complex two-dimensional model should reach the same conclusions regarding the luminosity of IRS1 and IRS3. Prediction of the envelope’s inner radii, on the other hand, is a less robust conclusion. The central protostar’s spectrum does have a large impact on the inner radius required to match the data. However, the models do suggest that the inner radius of IRS1 is much larger than the inner radius of IRS3. These results still hold even when the disk is altered or scattering is included in the model.

Finally, IRS1 and IRS2, the potentially binary companion to IRS1, show different SEDs. IRS1 is detected at submillimeter wavelengths, while IRS2 shows no clear evidence of long-wavelength emission. Possibly, IRS2 is more evolved than IRS1 and has stopped accreting material from the surrounding envelope. Perhaps, IRS1 and IRS2 exhibit such different properties because IRS1 is dominating the accretion. In fact, this might be common in binaries that are close enough; initially, one gets bigger and then dominates the accretion for the duration of their formation.

## 7. Acknowledgements

Support for this work, part of the *Spitzer* Legacy Science Program, was provided by NASA through contract 1224608 issued by the Jet Propulsion Laboratory, California Institute of Technology, under NASA contract 1407, and the Smithsonian Astrophysical Observatory, under NASA contract 1279198. This work was also supported by NASA grants NAG5-10488 and NNX07AJ72G. KEY was supported by NASA under Grant No. NGT5-50401 issued through the Office of Space Science. CHY thanks the Louisiana Board of Regents, BoRSF, under agreement NASA/LEQSF(2001-2005)-LaSPACE and NASA/LaSPACE under grant NGT5-40115 for support during this project.



## REFERENCES

- André, P., Motte, F., & Bacmann, A., 1999, *ApJ*, 513, L57
- Anglada, G. 1995, in *Circumstellar Disks, Outflows and Star Formation*, ed. S. Lizano & J. M. Torrelles (Rev. Mexicana Astron. Astrofis. Ser. Conf. 1)(México, D.F.: Inst. Astron. Univ. Nac. Autónoma México), 67
- Bourke, T.L., 2001, *ApJ*, 554, L91
- Butner, H.M., Natta, A., & Evans, N.J. II, 1994, *ApJ*, 420, 326
- Caselli, P., Benson, P.J., Myers, P.C., & Tafalla, M., 2002, *ApJ*, 572, 238
- Chandler, C.J., Brogan, C.L., Shirley, Y.L., & Loinard, L., 2005, *ApJ*, 632, 371
- Chen, X., Bourke, T.L., Launhardt, R., & Henning, T., 2008, *ApJ*, 686, L107
- Chiang, E.I. & Goldreich, P., 1997, *ApJ*, 490, 368
- Curiel, S., Canto, J., & Rodríguez, L. F. 1987, *RMxAA*, 14, 595
- Curiel, S., Rodríguez, L. F., Bohigas, J., Rith, M., & Cantó, J. 1989, *Astrophys. Lett. Comm.*, 27, 299
- De Vries, C.H., et al., in preparation
- Draine, B.T. & Lee, 1984, *ApJ*, 285, 89
- Duchêne, G., Bontemps, S., Bouvier, J., André, P., Djupvik, A.A., & Ghez, A.A., 2007, *A&A*, 476, 229
- Dunham, M.M., et al., 2006, *ApJ*, 651, 945
- Dunham, M.M., Crapsi, A., Evans, N.J., II, Bourke, T.L., Huard, T.L., Myers, P.C., & Kauffmann, J., 2008, *ApJS*, 179, 249
- Dunham, M.M., et al., in preparation
- Evans, N.J. II, et al., 2003, *PASP*, 115, 965
- Evans, N.J. II, et al., 2007, Final Delivery of Data from the c2d Legacy Project: IRAC and MIPS (Pasadena:SSC), <http://peggysue.as.utexas.edu/SIRTF/>
- Fazio, G.G., et al., 2004, *ApJS*, 154, 10

- Greene, T.P., Wilking, B.A., Andre, P., Young, E.T., & Lada, C.J., 1994, *ApJ*, 434, 614
- Harvey, P., et al. 2006, *ApJ*, 644, 307
- Harvey, P., et al. 2007, *ApJ*, 663, 1149
- Hodapp, K.-W., *ApJS*, 94, 615
- Ivezić, Ž., Nenkova, M., & Elitzur, M., 1999, *astro-ph/9910475*
- Jørgensen, J.K., Lahuis, F., Schoier, F.L., van Dishoeck, E.F., Blake, G.A., Boogert, A.C.A., Dullenmond, C.P., Evans, N.J. II, Kessler-Silacci, J.E., & Pontoppidan, K.M., 2005, *ApJ*, 631, L77
- Jørgensen, J.K., Schoier, F.L., & van Dishoeck, E.F., 2004, *A&A*, 416, 603
- Jørgensen, J.K., 2004, *A&A*, 424, 589
- Kenyon, S.J. & Hartmann, L., 1987, *ApJ*, 323, 714
- Lada, C.J., 1987, *IAUS*, 115, 1
- Lee, C-F. & Ho, P.T.P., 2005, *ApJ*, 632, 964
- Lee, C.-F., Mundy, L.G., Stone, J.M., & Ostriker, E.C., 2002, *ApJ*, 576, 294
- Lee, J.-E., Di Francesco, J., Lai, S.-P., Bourke, T.L., Evans, N.J., II, Spiesman, B., Myers, P.C., Allen, L.E., Brooke, T.Y., Porras, A., & Wahhaj, Z., 2006, *ApJ*, 648, 491
- Loinard, L., Chandler, C.J., Rodriguez, L.F., D'Alessio, P., Borgan, C.L., Wilner, D.J., & Ho, P.T.P., 2007, *ApJ*, 670, 1353
- Lonsdale, C., et al., 2003, *PASP*, 115, 897
- Lynds, B.T., 1962, *ApJS*, 7, 1
- Motte, F. & André, P., 2001, *A&A*, 365, 440
- Myers, P.C. & Ladd, E.F., 1993, *ApJ*, 413, L47
- Noriega-Crespo, A., et al., 2004, *ApJS*, 154, 352
- Ossenkopf, V. & Henning, T., 1994, *A&A*, 291, 943
- Rieke, G.H., et al., 2004, *ApJS*, 154, 25

- Rodríguez, L. F. & Reipurth, B., 1998, *RMxAA*, 34, 13
- Schechter, P.L., Mateo, M., & Saha, A., 1993, *PASP*, 105, 1342
- Shang, H., Lizano, S., Glassgold, A., & Shu F. 2004, *ApJ*, L69
- Shirley, Y. L., Claussen, M., Bourke, T. L., Young, C. H., & Blake, G. A. 2007, *ApJ*, 667, 329
- Shirley, Y.L., Evans, N.J. II, & Rawlings, J.M.C., 2002, *ApJ*, 575, 337
- Shu, F.H., Adams, F.C., & Lizano, S., 1987, *ARA&A*, 25, 23
- Terebey, S., Shu, F.H., & Cassen, P., 1984, *ApJ*, 286, 529.
- Umemoto, T., Hirano, N., Kameya, O., Fukui, Y., Kuno, N., & Takakubo, K., 1991, *ApJ*, 377, 510
- Werner, M.W., et al., 2004, *ApJS*, 154, 1
- Wu, J., Dunham, M.M., Evans, N.J. II, Bourke, T.L., & Young, C.H., 2007, *AJ*, 133, 1560
- Yonekura, Y., Dobashi, K., Mizuno, A., Ogawa, H., & Fukui, Y., 1997, *ApJS*, 110, 21
- Young, C.H., Shirley, Y.L., Evans, N.J., II, & Rawlings, J.M.C., 2003, *ApJS*, 145, 111
- Young, C.H., et al., 2004, *ApJS*, 154, 396
- Young, C.H. & Evans, N.J. II, 2005, *ApJ*, 627, 293
- Young, C.H., Bourke, T.L., Young, K.E., Evans, N.J., II, Jørgensen, J.K., Shirley, Y.L., van Dishoeck, E.F., & Hogerheijde, M., 2006, *AJ*, 132, 1998
- Yun, J.L. & Clemens, D.P., 1995, *AJ*, 109, 742

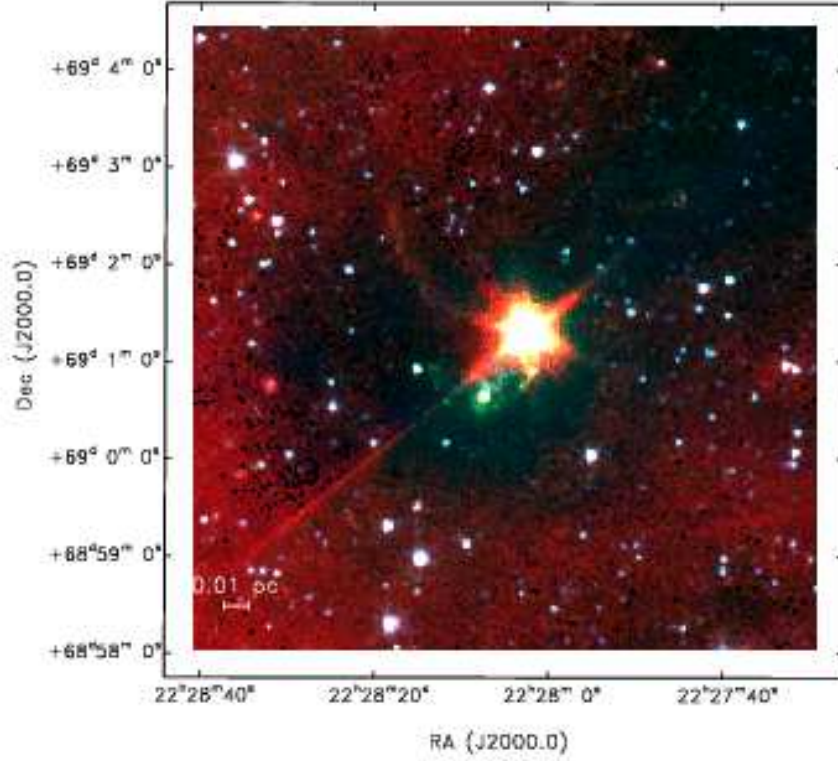


Fig. 1.— Three-color IRAC image of L1221. Red corresponds to  $8.0\ \mu\text{m}$ , green is  $4.5\ \mu\text{m}$ , and blue is  $3.6\ \mu\text{m}$ . The sources are labeled in Figure 3. IRS1/IRS2 is the brightest source; they appear unresolved because the source is overexposed in this image. IRS3 is the small, green object southeast of IRS1/2. An arc of emission extends from L1221-IRS1 to the northeast. L1221-IRS3 shows a signature of a north-south outflow.

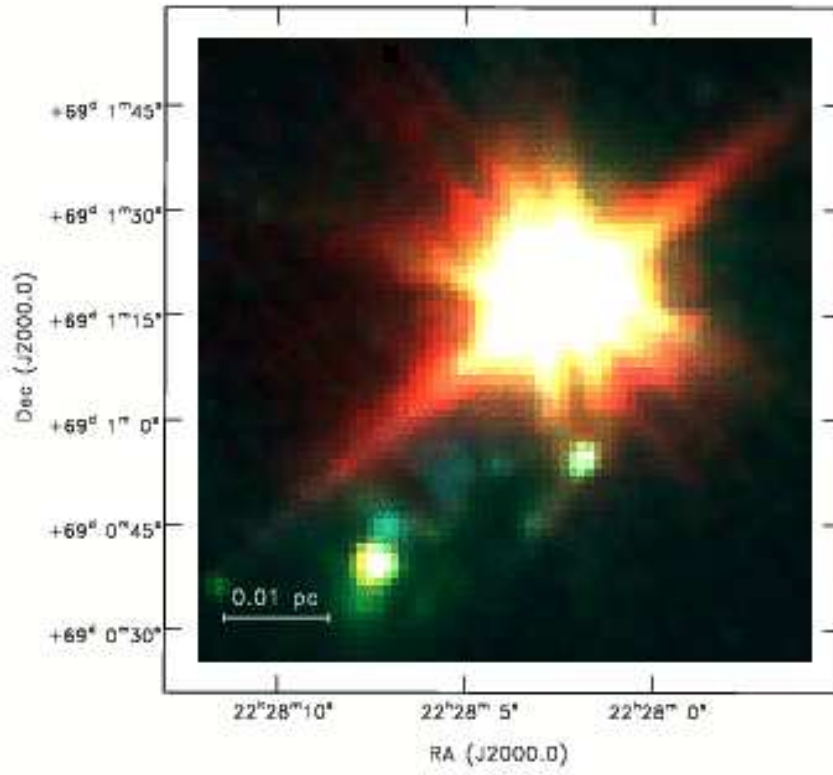


Fig. 2.— Three-color IRAC image of L1221. The color scheme is the same as in Figure 1; the image is zoomed in to show detail of the inner region. IRS1 and IRS2 are in the brightest source; they appear unresolved because the source is overexposed in this image. IRS3 is the green object southeast of IRS1/2.

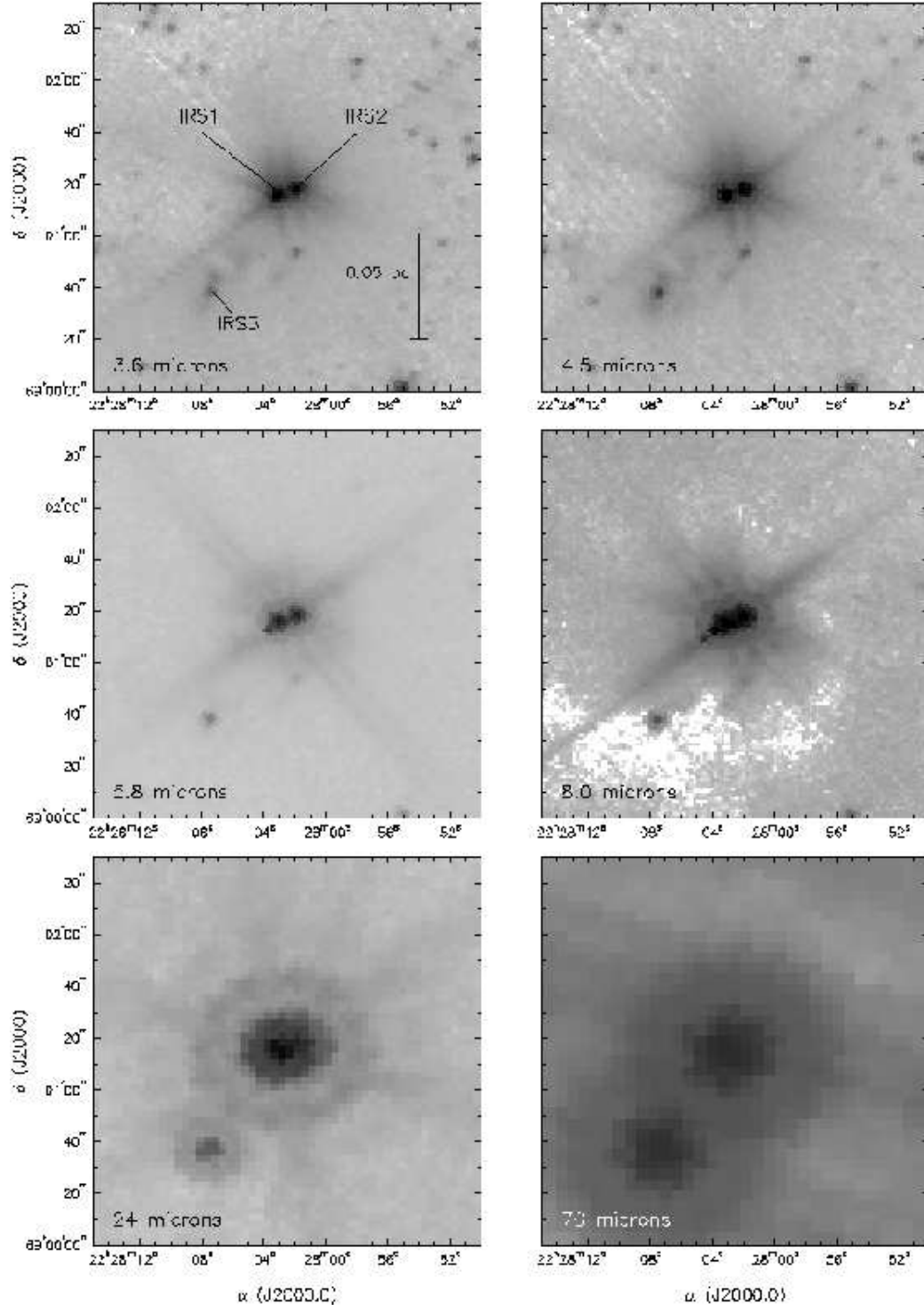


Fig. 3.— The IRAC and MIPS images are shown for L1221. The maps are shown with logarithmic scaling to show IRS1, IRS2, and IRS3.

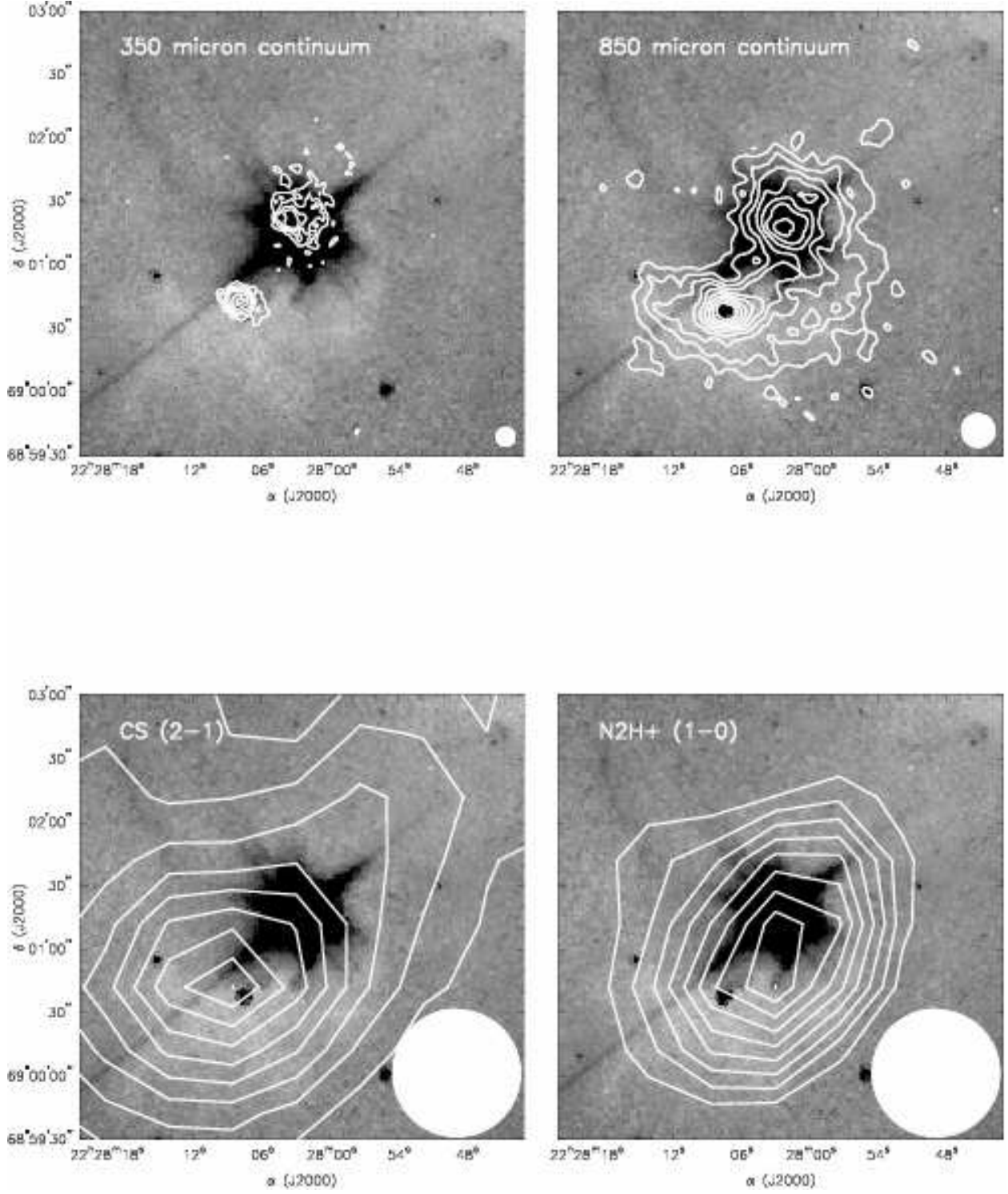


Fig. 4.— Millimeter observations are overlaid, as contours, on the 8  $\mu\text{m}$  greyscale image. The upper left panel shows 350  $\mu\text{m}$ , upper right is 850  $\mu\text{m}$ , the lower left panel has CS ( $J=2 \rightarrow 1$ ), and the lower right panel has N<sub>2</sub>H<sup>+</sup> ( $J=1 \rightarrow 0$ ).

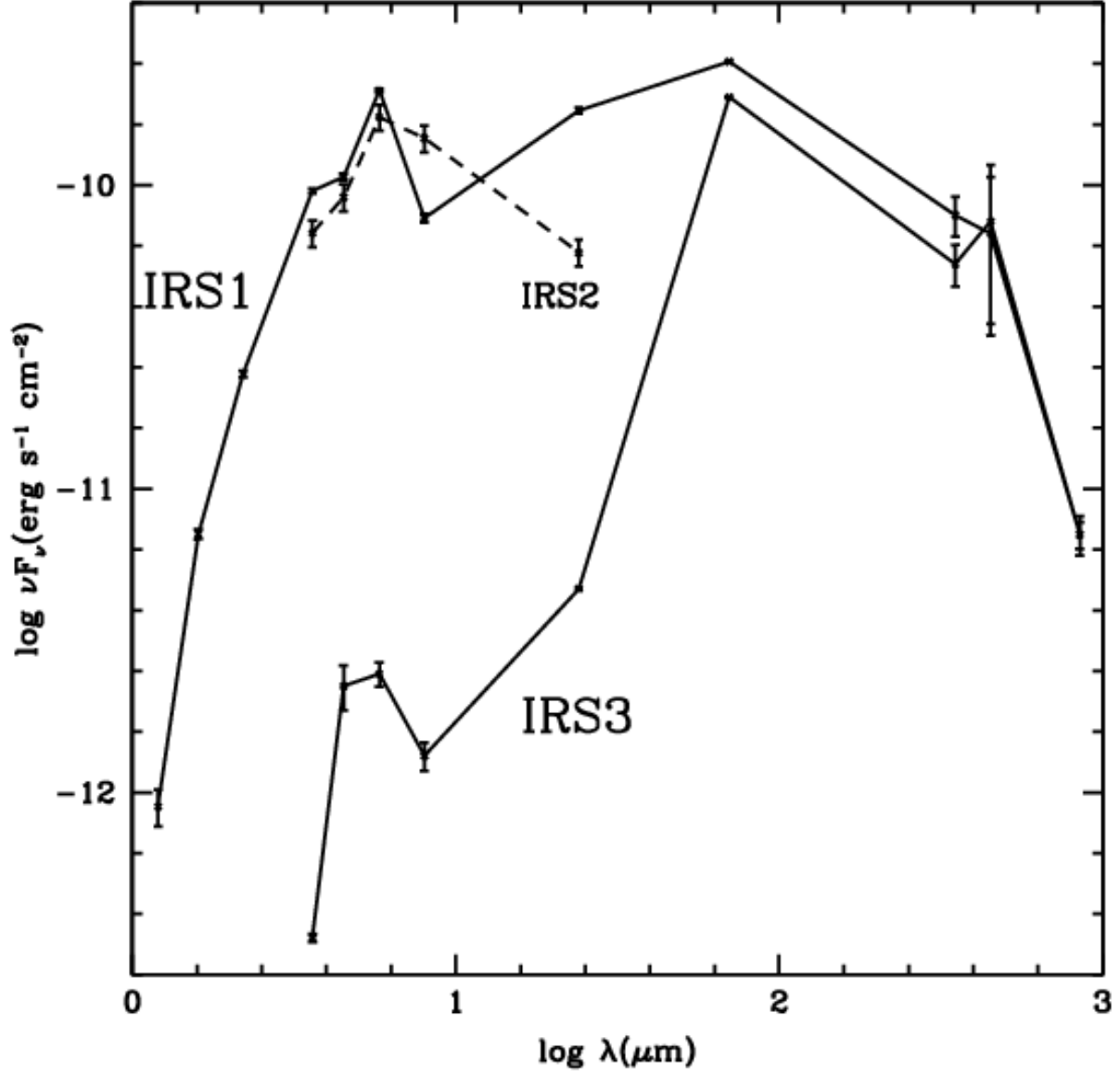


Fig. 5.— Spectral energy distributions for L1221-IRS1, IRS2, and IRS3. IRS1 and IRS3, shown as solid lines, were modelled while IRS2 (dashed line) was not.



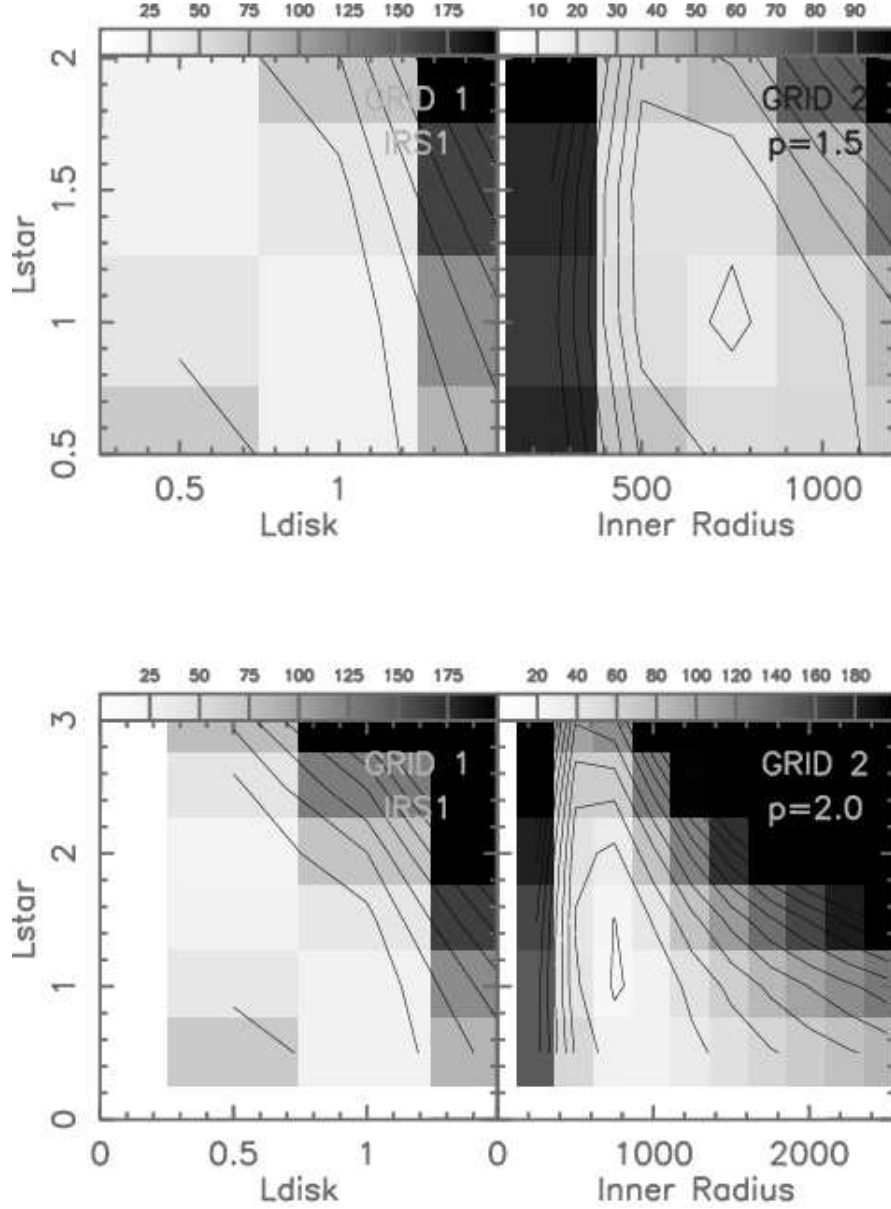


Fig. 6.— The  $\tilde{\chi}^2$  values for models of IRS1 with  $p = 1.5$  and  $p = 2.0$ . White areas denote lower  $\tilde{\chi}^2$  values. The default values, except when allowed to vary, are  $L_* = 1.0 L_\odot$ ,  $L_D = 1.0 L_\odot$ ,  $r_i = 1000$  AU, and  $T_* = 3000$  K.

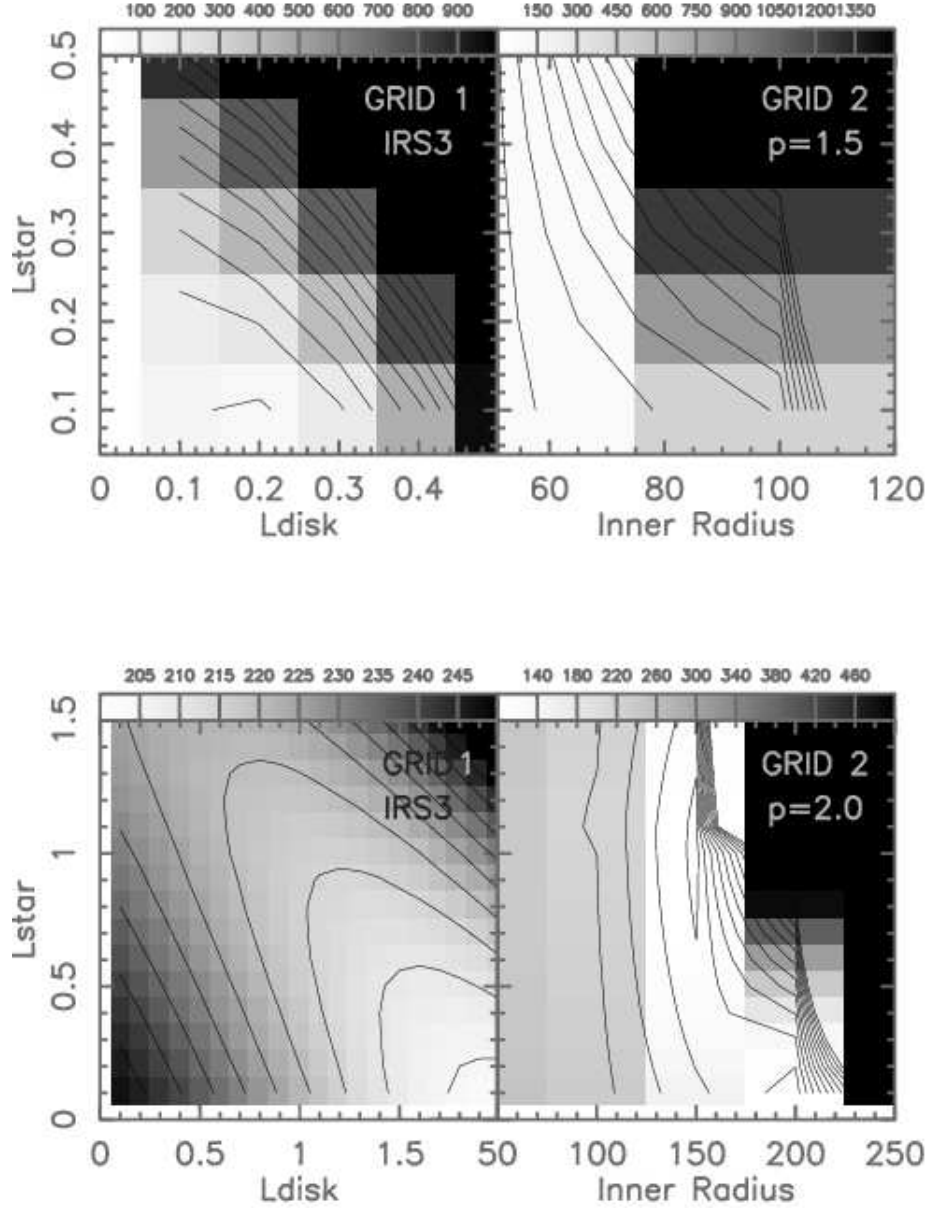


Fig. 7.— The  $\tilde{\chi}^2$  values for models of IRS3 with  $p = 1.5$  and  $p = 2.0$ . White areas denote lower  $\tilde{\chi}^2$  values. The default values, except when allowed to vary, are  $L_* = 0.4 L_{\odot}$ ,  $L_D = 0.4 L_{\odot}$ ,  $r_i = 100$  AU, and  $T_* = 3000$  K.

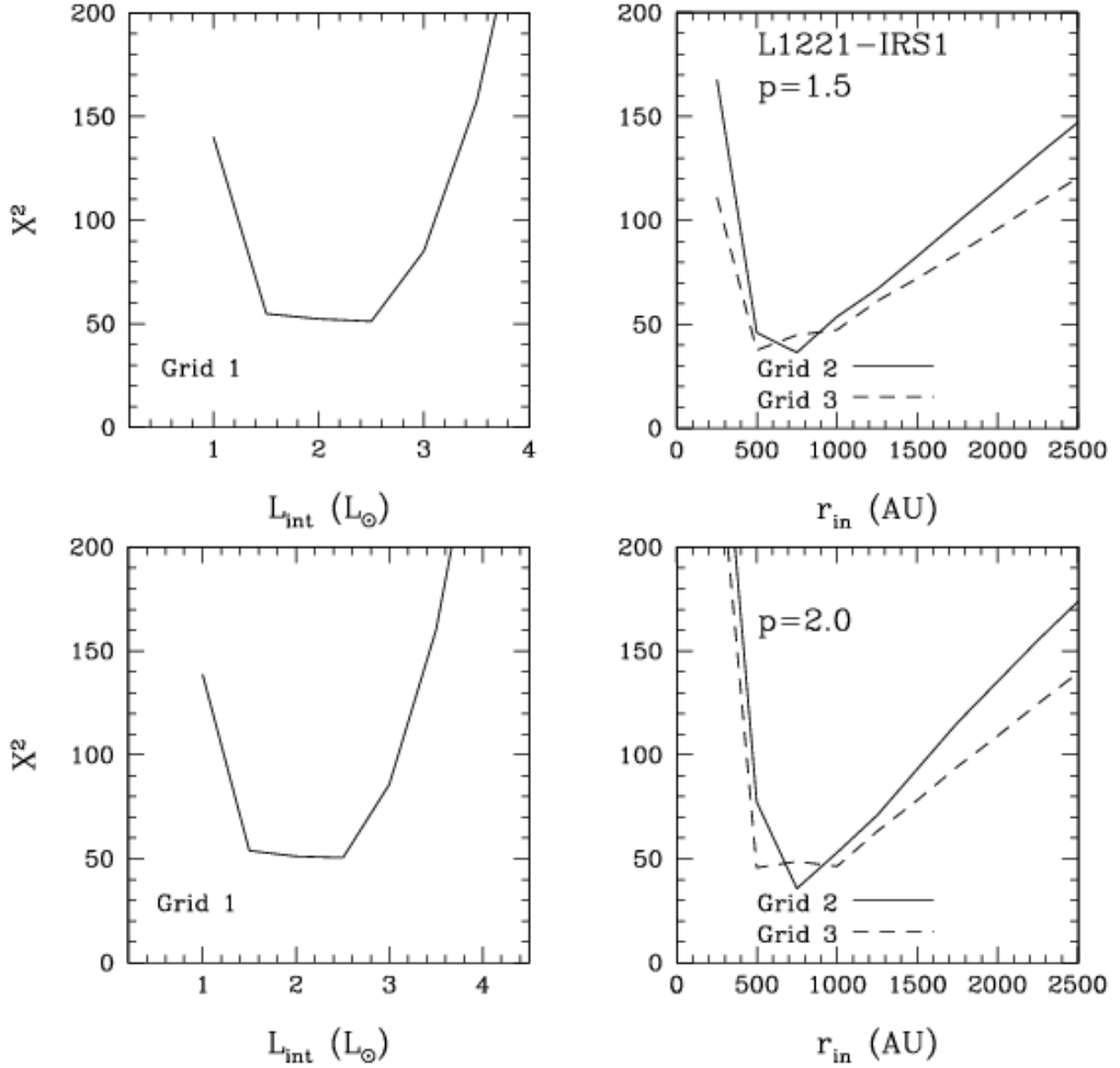


Fig. 8.— The minimum  $\tilde{\chi}^2$  values plotted from the data shown in Figure 6.

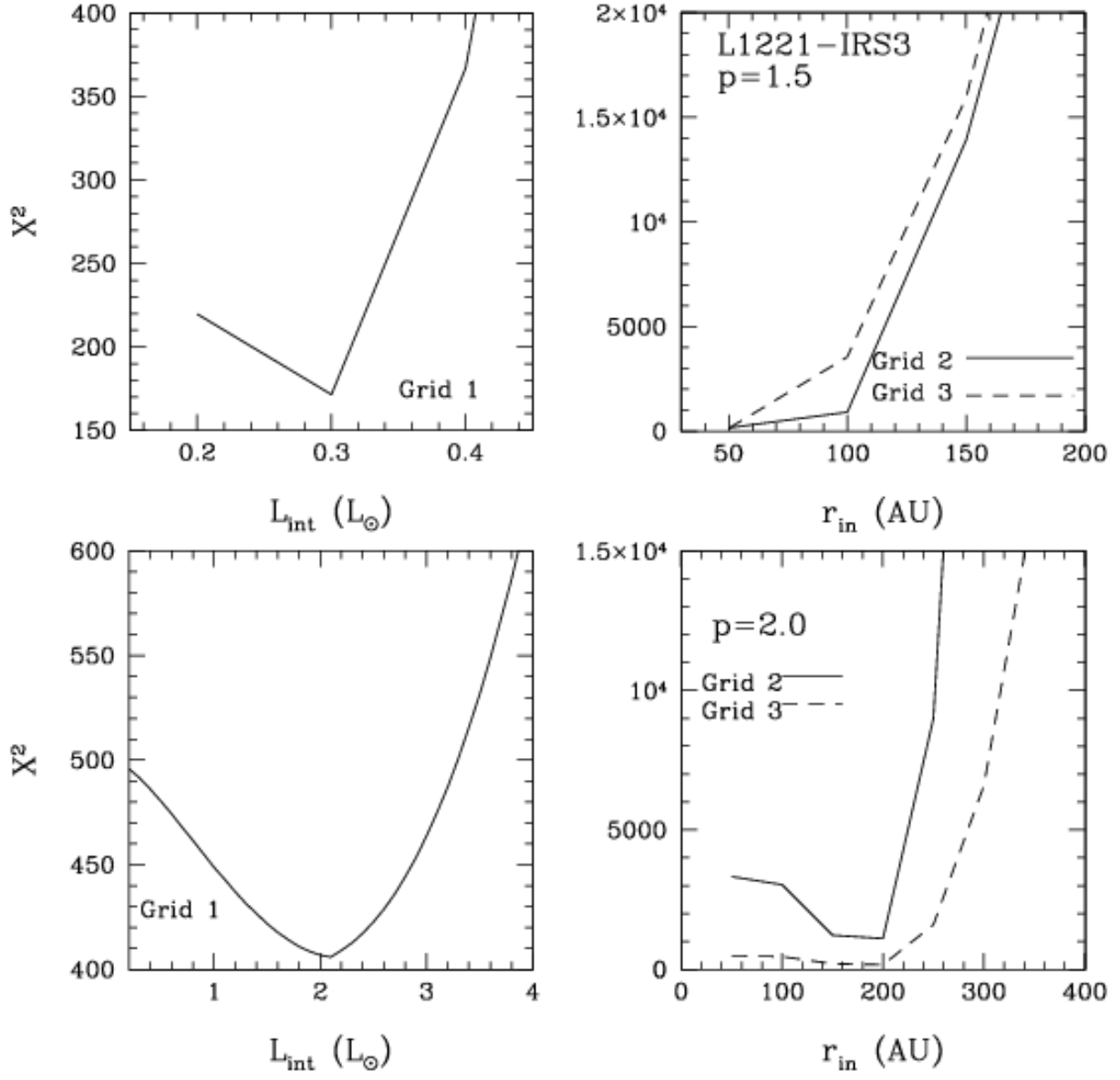


Fig. 9.— The minimum  $\tilde{\chi}^2$  values plotted from the data shown in Figures 7.

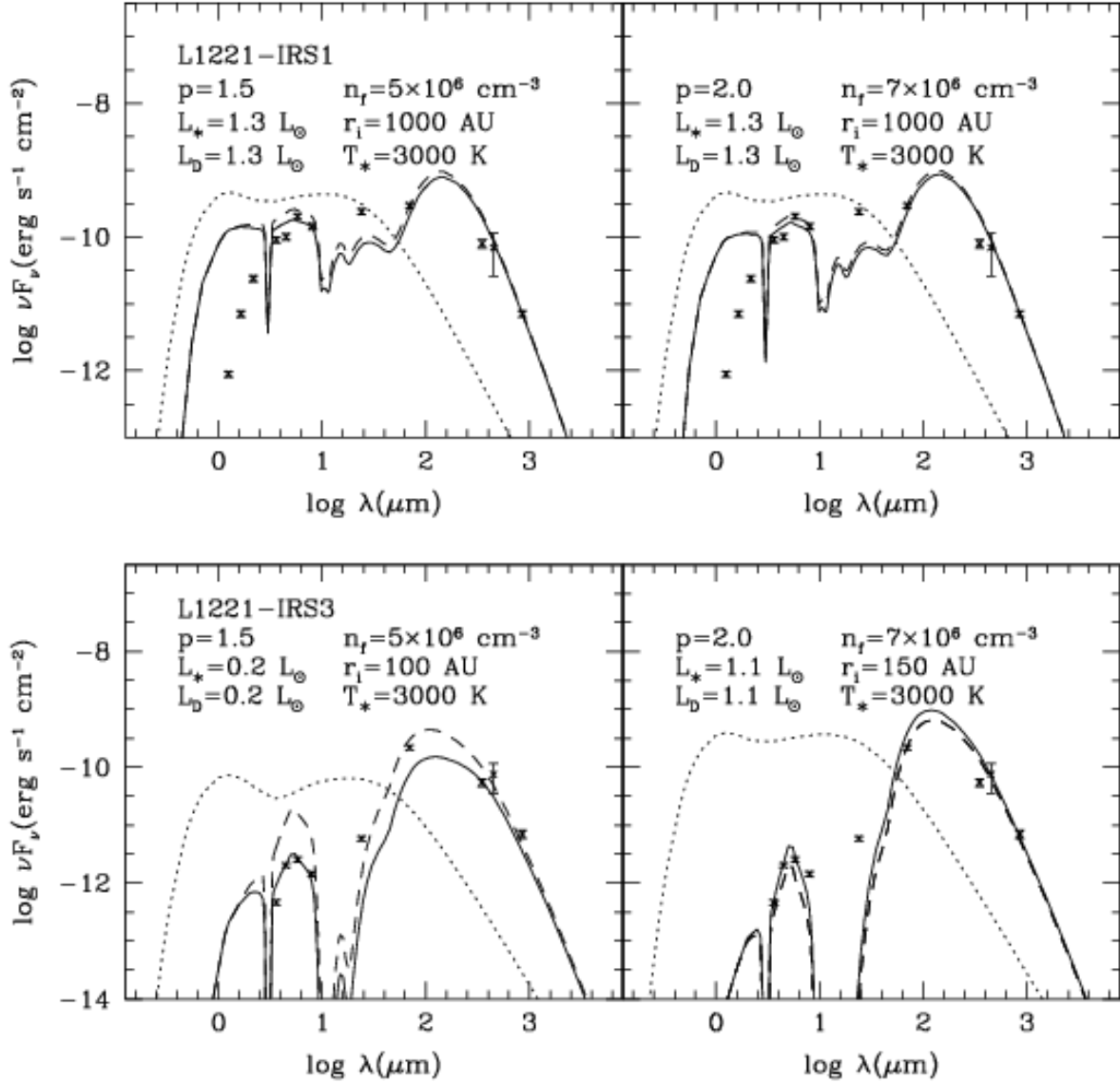


Fig. 10.— The best-fit models for differing power-law indices have different parameters as shown in this figure for both L1221-IRS1 and L1221-IRS3. Best-fit parameters are in Table 2. The dotted line represents the SED of the star and disk; the solid line is the SED of the star, disk, and envelope. The dashed line is the model that best-fits only the MIPS observations. The error bars are the observed fluxes.

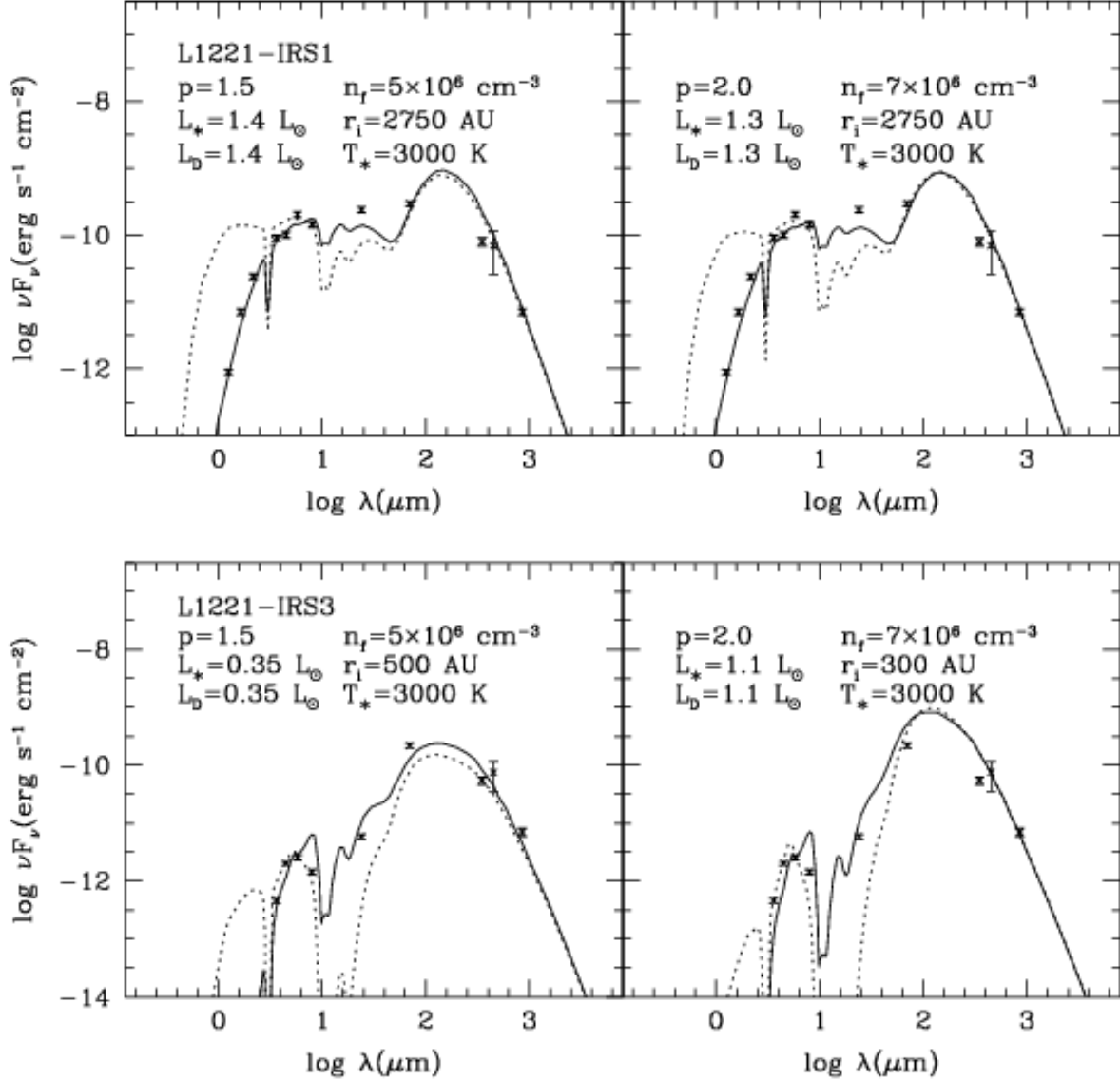


Fig. 11.— The effects of scattering have been included in the SEDs shown in this figure. The dotted line shows the models from Figure 10 while the solid line shows best-fit models when scattering is included. The parameters for these best-fit models are as labeled here. The internal luminosity is mostly independent of the inclusion of scattering; the inner radii increase by a factor of 2 or more when scattering is included.

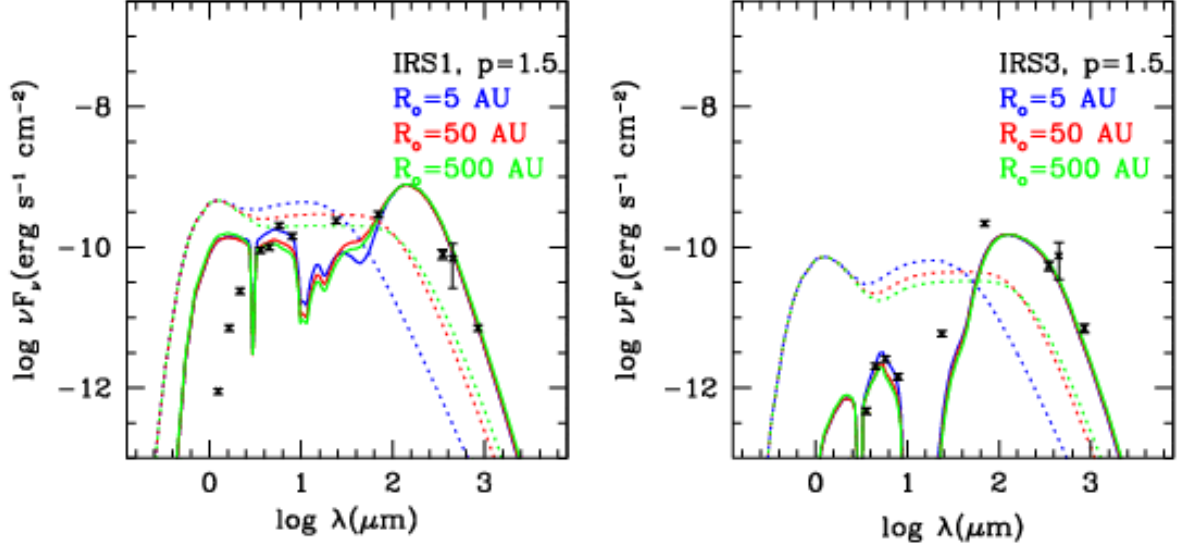


Fig. 12.— SEDs for IRS1 and IRS3 ( $p = 1.5$ ) in which the disk outer radius has been changed. The blue shows the SED with  $R_o = 5$  AU, red is  $R_o = 50$  AU, and green is  $R_o = 500$  AU. Black error bars are the observed data.

Table 1. Spectral Energy Distribution

Source Name	Lambda $\mu\text{m}$	$F_\nu$ mJy	Aperture arcsec
SSTc2d J222803.0+690117	1.25	0.374 $\pm$ 0.037	2.5
(L1221-IRS1)	1.65	3.91 $\pm$ 0.39	2.5
$L_{bol}^{obs}=1.8 L_\odot$	2.17	17.3 $\pm$ 1.7	2.5
$T_{bol}^{obs}=250 \text{ K}$	3.6	109 $\pm$ 11	1.7 <sup>a</sup>
$\alpha = 0.81$	4.5	149 $\pm$ 15	1.7 <sup>a</sup>
	5.8	392 $\pm$ 39	1.9 <sup>a</sup>
	8.0	387 $\pm$ 39	2.0 <sup>a</sup>
	24	1940 $\pm$ 187	5.7 <sup>a</sup>
	70	6940 $\pm$ 641	17 <sup>a</sup>
	350	9300 $\pm$ 1400	40
	450	10400 $\pm$ 6500	40
	850	2000 $\pm$ 200	40
SSTc2d J222801.8+690119	3.6	83.6 $\pm$ 8.4	1.7 <sup>a</sup>
(L1221-IRS2)	4.5	137 $\pm$ 14	1.7 <sup>a</sup>
$L_{bol}^{obs}=0.4 L_\odot$	5.8	324 $\pm$ 32	1.9 <sup>a</sup>
$T_{bol}^{obs}=450 \text{ K}$	8.0	381 $\pm$ 38	2.0 <sup>a</sup>
$\alpha = -0.05$	24	368 $\pm$ 35	5.7 <sup>a</sup>
	70	< 300	17 <sup>a</sup>
SSTc2d J222807.4+690039	3.6	0.567 $\pm$ 0.060	1.7 <sup>a</sup>
(L1221-IRS3)	4.5	3.1 $\pm$ 0.3	1.7 <sup>a</sup>
$L_{bol}^{obs}=0.8 L_\odot$	5.8	4.96 $\pm$ 0.50	1.9 <sup>a</sup>
$T_{bol}^{obs}=68 \text{ K}$	8.0	3.84 $\pm$ 0.4	2.0 <sup>a</sup>
$\alpha = 0.99$	24	47.5 $\pm$ 4.4	5.7 <sup>a</sup>
	70	5080 $\pm$ 469	17 <sup>a</sup>
	350	6400 $\pm$ 1000	40
	450	11300 $\pm$ 6100	40
	850	2000 $\pm$ 300	40
SSTc2d J222815.1+685930	3.6	0.208 $\pm$ 0.02	1.7 <sup>a</sup>
	4.5	0.284 $\pm$ 0.03	1.7 <sup>a</sup>
$L_{bol}^{obs}=0.003 L_\odot$	5.8	0.38 $\pm$ 0.04	1.9 <sup>a</sup>
$T_{bol}^{obs}=187 \text{ K}$	8.0	0.613 $\pm$ 0.06	2.0 <sup>a</sup>
$\alpha = 0.25$	24	2.13 $\pm$ 0.27	5.7 <sup>a</sup>
	70	24.1 $\pm$ 3.8	17 <sup>a</sup>

<sup>a</sup>FWHM of the *Spitzer point-spread profile*.



Table 2. Model Parameters

	Parameter	Accepted Value
L1221-IRS1	$p$	1.5
	$n_f$	$5 \times 10^6 \text{ cm}^{-3}$
	$r_i$	1000 AU
	$L_{int}$	$2.6 L_{\odot}$
	$T_*$	3000 K
L1221-IRS1	$p$	2.0
	$n_f$	$7 \times 10^6 \text{ cm}^{-3}$
	$r_i$	1000 AU
	$L_{int}$	$2.6 L_{\odot}$
	$T_*$	3000 K
L1221-IRS3	$p$	1.5
	$n_f$	$5 \times 10^6 \text{ cm}^{-3}$
	$r_i$	100 AU
	$L_{int}$	$0.4 L_{\odot}$
	$T_*$	3000 K
L1221-IRS3	$p$	2.0
	$n_f$	$7 \times 10^6 \text{ cm}^{-3}$
	$r_i$	150 AU
	$L_{int}$	$2.2 L_{\odot}$
	$T_*$	3000 K